Supporting Information for

Role of poroelasticity during the early postseismic deformation of the 2010 Maule megathrust earthquake

Carlos Peña[1,2], Sabrina Metzger[1], Oliver Heidbach[1,3], Jonathan Bedford[1], Bodo Bookhagen[2], Marcos Moreno[4], Onno Oncken[1,5], and Fabrice Cotton[1,2]

[1] Helmholtz Centre Potsdam, GFZ German Research Centre for Geosciences, Potsdam, Germany

[2] Institute of Geosciences, University of Potsdam, Germany

[3] Institute of Applied Geosciences, Technical University Berlin, Germany

[4] Departamento de Geofísica, University of Concepción, Chile

[5] Department of Earth Sciences, Freie Universität Berlin, Berlin, Germany

Corresponding author: carlosp@gfz-potsdam.de

Contents of this file

1.- Geodetic observations

Fig. S1a shows the uncertainty that results both in the GNSS horizontal and vertical component. In the vertical component, the uncertainty represents about 40% of the overall vertical signal. The uncertainty for the horizontal component is much smaller, representing approximately 10% of the total signal only. Before the afterslip inversion, we removed a linear ramp from the InSAR data as explained in the main text using the GNSS data. This approach produces a good agreement between the GNSS displacements, collapsed into line-of-sight, and the InSAR displacements (Figure S1b).

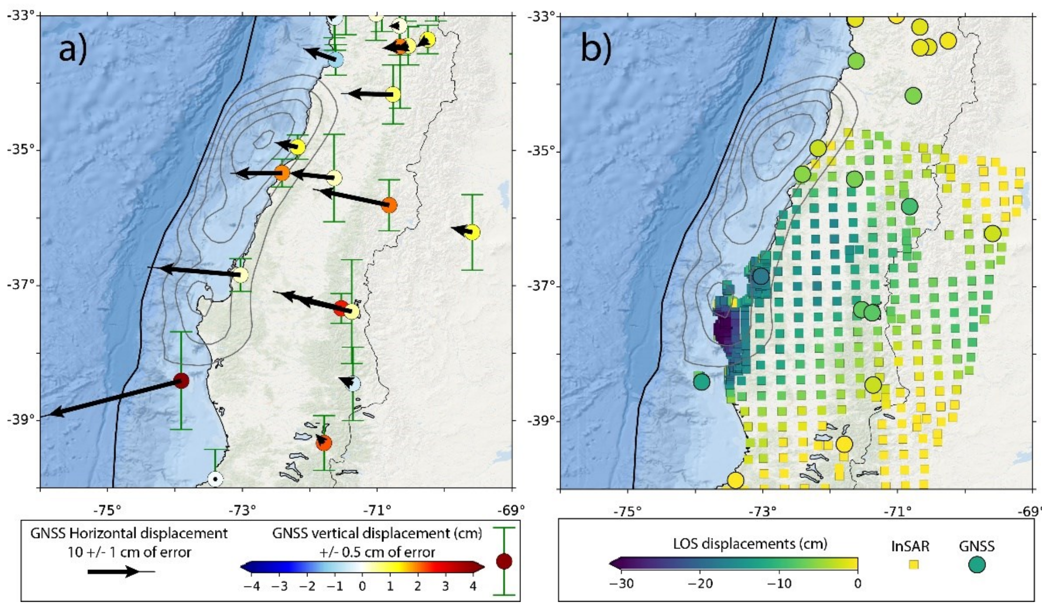

Figure S1. Horizontal and vertical GNSS data uncertainty (a) and deramped InSAR, and GNSS displacements, collapsed into LOS (b).

2.- Model geometry

We use the 4D model geometry of Peña et al. (2020). The model incorporates the slab geometry of Hayes et al. (2012) and the Moho discontinuity from Tassara et al. (2006). It extends 4000 km in West-East, 2000 km in North-South and 400 km in the vertical direction (Fig. 3 in Peña et al., 2020). This is large enough to avoid artefacts due to model boundary conditions. The model volume is discretized into 2,350,000 finite elements with a higher resolution close to the area of expected postseismic deformation (~3 km) and coarser resolution (~50 km) at the model boundaries. To initiate the postseismic deformation we simulate the coseismic rupture of the Maule M_w 8.8 earthquake using the coseismic slip model from Moreno et al. (2012) on a fault that is ~700 km long in strike direction and ~90 km deep. The relative displacement of the hanging and foot walls is governed by linear constraint equations that satisfy the specified slip at each node (Masterlark, 2003).

3.- F-test

We calculate the p-values by first computing the F-values as follows:

$$F = \frac{(S_1^2 - S_2^2) \times df_2}{(df_1 - df_2) \times S_2^2}$$

where S_1^2 and S_2^2 represent the residual sum of the squares of the model of the model with fewer and higher model parameters, respectively, while df_1 and df_2 are the degrees of freedom associated to these modes, respectively, and calculated as N – P, with N representing number of data samples and P the number of model parameters (e.g., Press et al., 2002). We perform two calculations by comparing the model results from 1) the poro-viscoelastic and the elastic-only models and 2) the poro-viscoelastic model and (non-linear) viscoelastic-only model. The latter, in particular, compare to what extend the implementation of poroelasticity is statistically significant given the small geodetic data fit improvement is not conclusive. We thus consider in 1) and 2) as null hypotheses as the elastic-only and viscoelastic-only models, i.e., that the implementation of poro-viscoelasticity and poroelasticity, respectively, does not provide a significant better improvement. We use the python function *scipy.stats.f.sf* to obtain the p-values based on the calculated F-value. For the case 1) we find an F-value = 7.87 and for case 2) an F-value = 1.28, yielding to p-values of 3.27×10^{-129} and 6.6×10^{-4}, respectively. These small values are in good agreement with those resulting from studies considering highly dense geodetic measurements (e.g., Lin et al., 2010). These p-value are considerably smaller than a significance level of 0.05, and therefore the null hypotheses are rejected.

4.- Afterslip inversion

The afterslip inversion is obtained after removing the poroelastic and viscoelastic component to the geodetic data (see main text). We then apply an afterslip inversion approach considering the following constraints: 1) back-slip is not allowed, 2) the rake vector angle is constrained to occur in the up-dip direction between 60° and 120° (this mostly agrees with the rake of aftershocks during the early postseismic deformation, e.g., Lange et al., 2012), and 3) smoothing Laplacian constraints (e.g., Bedford et al., 2013; Peña et al., 2020). We test different relative weighting of the InSAR and GNSS data sets following Cavalié et al. (2013) using the model considering poro-viscoelasticity. Here, we find that a relative weight of 0.6 can best explain both data sets as displayed in Figure S2. To be able to directly compare our results, we use the same relative weight factor for all afterslip inversions, i.e., using a fully elastic and poroelastic model. To reduce computation time to generate the Green's functions, we group nodes within a moving spatial window of 10×10 km^2 along the fault interface (e.g., Li et al., 2015).

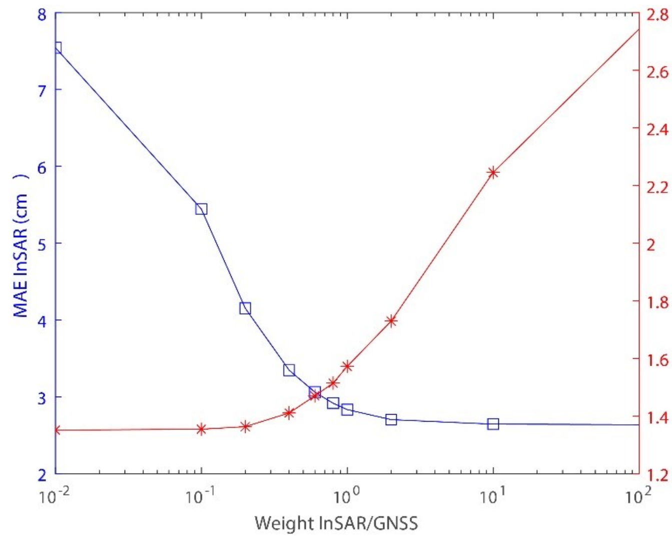

Figure S2. Misfit functions of InSAR and GNSS data using a varying relative weight. MAE means mean absolute error.

5. Coupled versus uncoupled model tests

In the coupled model (Figure S3a), the afterslip distribution obtained after removing the visco-poroelastic effects (Figure 5a in the main text) is implemented as a displacement boundary condition on the model fault interface along with poroelasticity and viscoelasticity through a forward simulation to model the simultaneous surface displacement response to the three postseismic processes investigated in this study. In contrast, the uncoupled model (Figure S3b) is the sum of the individual contributions from each postseismic process to the surface displacement field. Note that the differences in Figure S3c are relatively small and lower than the uncertainty of the GNSS data of approximately 10% in the horizontal and up to 40% in the vertical.

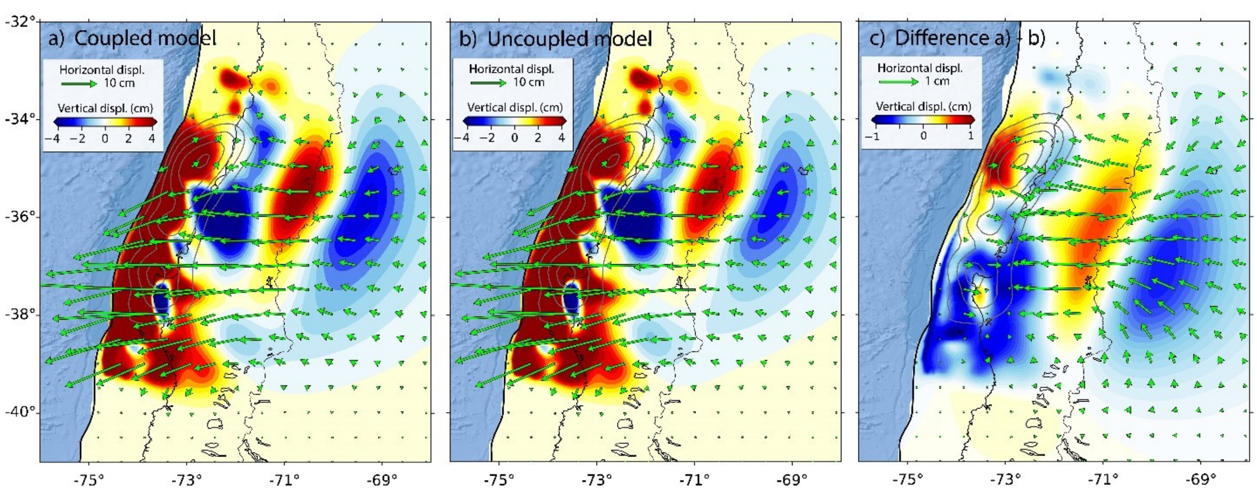

Figure S3. Cumulative 3D surface displacement field from model coupling tests.

6. Afterslip uncertainty and resolution test model

We compute the afterslip standard deviation using bootstrapping tests after randomly removing 10% of the geodetic data with replacement for 200 iterations (e.g., Melgar et al., 2017). At the location of the largesr poroelastic effects (black rectangles in Figure S4) we find that the afterslip differences can reach ±25 cm, which is at least six times larger than the mean afterslip standard deviation resulting from bootstrapping tests (Figure S4c). We also compute the resolution and spread (after)slip model following Williamson and Newman (2018) (Figure S5). The resolution **R** is calculated as **R** = $[\, G^TG + \epsilon^2 I \,]^{-1}\, G^TG$ where G represents the Green's function matrix, I the identity matrix, and ϵ a weighting smoothing parameter. The spread model S is obtained as **S** = L/√R, with L=10 km as the sub-fault length. The diagonal of **R** provides information about how well afterslip on each fault patch is resolved, given the data kernel and a priori model inputs, ranging from 1 (perfectly resolved) to 0 (unresolved), while **S** the size of the minimum features that can be resolved. In the region where poroelastic processes play a significant role on afterslip distributions (black rectangles in Fig. S4), our model provides a high resolution (> 0.3, Figure 5a), and afterslip patches as small as 10-20 km can be identified (Figure S5c). The tests also show that both the resolution and spread model considerably increase when including InSAR data.

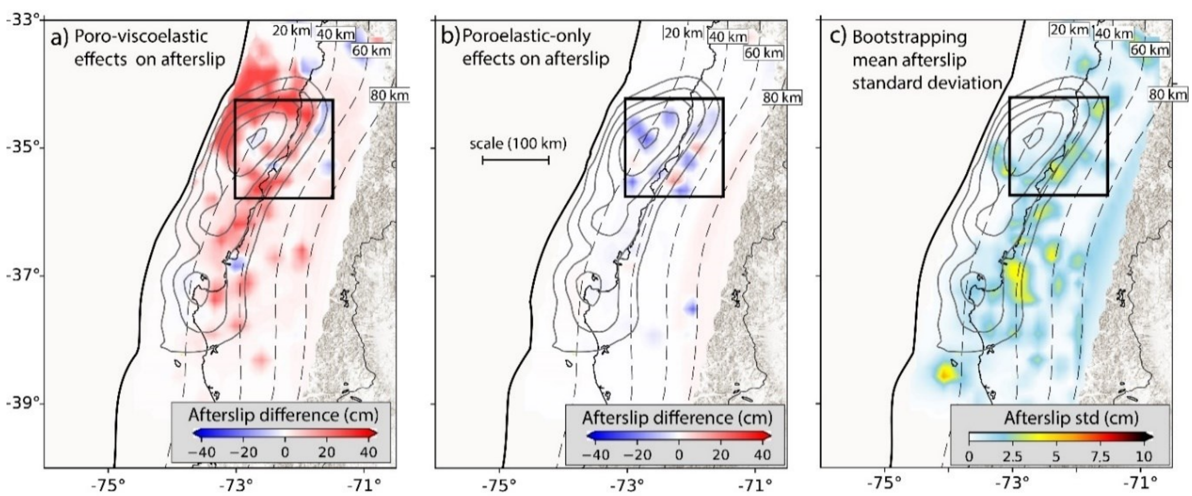

Figure S4. Afterslip uncertainty. Afterslip differences in a) and b) correspond to Fig. 4d and 4e in the main text, respectively.

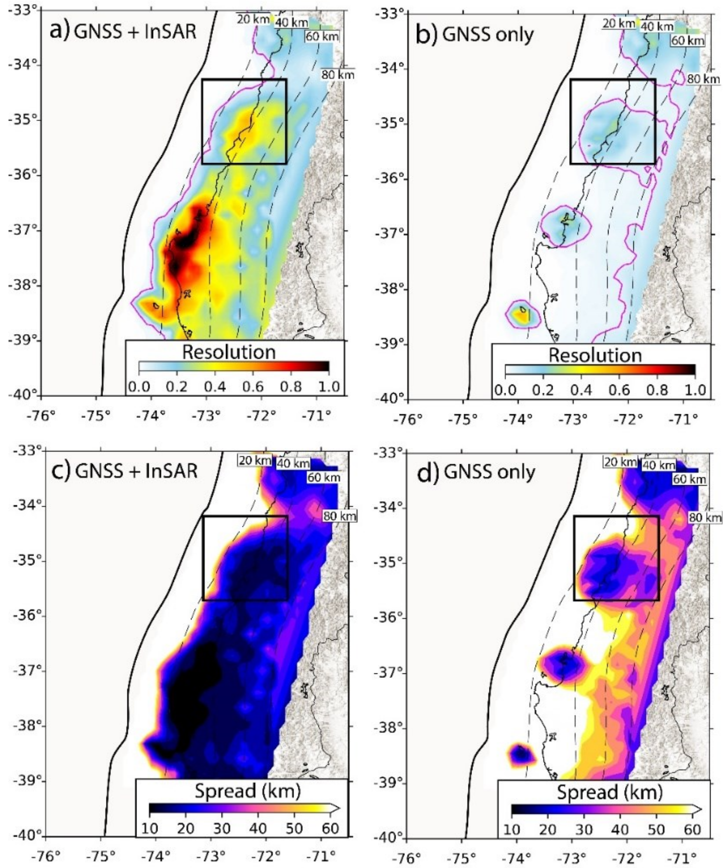

Figure S5. Resolution and spread model tests calculated on the fault interface. Resolution considering GNSS only (a) and GNSS plus InSAR (b). Spread considering GNSS only (c) and GNSS plus InSAR (d). Magenta contour lines in a) and b) exhibit a critical value of 0.1.

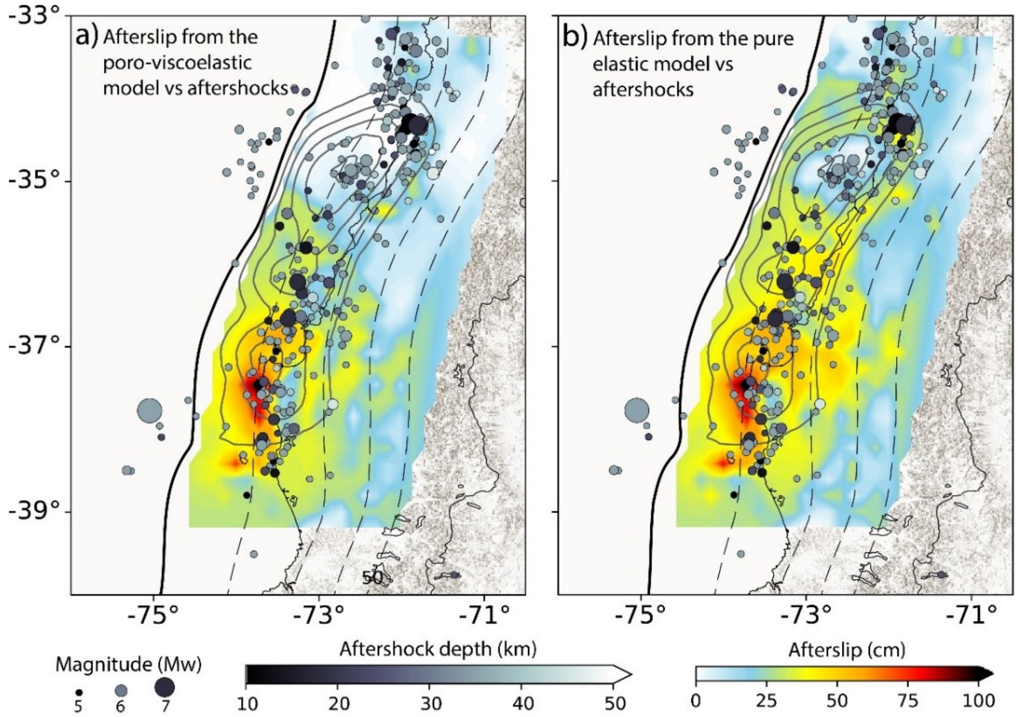

Figure S6. Spatial distribution of modeled afterslip versus observed aftershocks (Mw ≥ 5).

Table S1. Elastic properties and dislocation creep parameters.

Rock type [b]	**Young's modulus E [GPa]** [a]	**Poisson's ratio ν** [a]	**Pre-exponent A [MPa^{-n} s^{-1}]** [b]	**Stress exponent n** [b]	**Activation energy Q [kJ mol^{-1}]** [b]
Wet quartzite	100	0.265	3.2×10^{-4}	2.3	154
Wet olivine 1*	160	0.25	5.6×10^{6}	3.5	480
Wet olivine 2*	160	0.25	1.6×10^{5}	3.5	480
Diabase	120	0.3	2.0×10^{-4}	3.4	260

[a] Reference source from Christensen (1996) and Moreno et al. (2012)

[b] Reference source from Hirth and Kohlstedt (2003), Ranalli (1997)

* Wet olivine 1 and 2 contain 0.1 and 0.005% of water, respectively.

Table S2. Poroelastic parameters.

Rock type	Shear modulus E [GPa]	Poison's ration[a]	Permeability [m^2]	Voigt ratio [c]	Porosity [%] [c]
Poroelastic 1	100	0.265	1×10^{-14}	0.01	1
Poroelastic 2	100	0.265	1×10^{-16}	0.01	1

[c] Reference source from Wang (2000).

Table S3. Simulation configuration. MAE represents the mean absolute error.

Simulation	Continental crust	Continental mantle	Upper crust	MAE [cm]
1	Wet quartzite	Wet olivine 1	Poroelastic 1	5.4
2	Wet quartzite	Wet olivine 1	Poroelastic 2	5.6
3	Wet quartzite	Wet olivine 2	Poroelastic 1	5.7
4	Wet quartzite	Wet olivine 2	Poroelastic 2	5.8
5	Diabase	Wet olivine 1	Poroelastic 1	5.7
6	Diabase	Wet olivine 1	Poroelastic 2	5.9
7	Diabase	Wet olivine 2	Poroelastic 1	6.1
8	Diabase	Wet olivine 2	Poroelastic 2	6.2

References

Bedford, J., Moreno, M., Baez, J.C., Lange, D., Tilmann, F., Rosenau, M., et al. (2013). A high-resolution, time-variable after slip model for the 2010 Maule Mw = 8.8, Chile megathrust earthquake, Earth Planet. Sci. Lett., 383, 26–36. https://doi.org/10.1016/j.epsl.2013.09.020

Christensen, N. (1996). Poisson's ratio and crustal seismology. J. Geophys. Res.101 (B2), 3139–3156. https://doi.org /10.1029/95JB03446.

Hirth, G., & Kohlstedt, D. (2003). Rheology of the upper mantle and the mantle wedge: A view from the experimentalists. Inside the subduction Factory, 83-105. https://doi.org/10.1029/138GM06

Lange, D., Tilmann, F., Barrientos, S.E., Contreras-Reyes, E., Methe, P., Moreno, M., Heit, B., Agurto, H., Bernard, P., Vilotte, J.-P., Beck, S. (2012). Aftershock seismicity of the 27 February 2010 Mw 8.8 Maule earthquake rupture zone. Earth Planet. Sci. Lett.317–318, 413–425. https://doi org /10.1016 /j.epsl .2011.11.034.

Li, S., Moreno, M., Bedford, J., Rosenau, M., and Oncken, O. (2015), Revisiting viscoelastic effects on interseismic deformation and locking degree: A case study of the Peru-North Chile subduction zone. J. Geophys. Res. Solid Earth, 120, 4522– 4538. doi: 10.1002/2015JB011903.

Lin, Y. N., Kositsky, A. P., and Avouac, J.-P. (2010). PCAIM joint inversion of InSAR and ground-based geodetic time series: Application to monitoring magmatic inflation beneath the Long Valley Caldera, Geophys. Res. Lett., 37, L23301, doi:10.1029/2010GL045769.

Masterlark, T. (2003). Finite element model predictions of static deformation from dislocation sources in a subduction zone: sensitivities to homogeneous, isotropic, Poisson-solid, and half-space assumptions. J.Geophys. Res., Solid Earth108 (B11). https://doi .org /10 .1029 /2002JB002296.

Melgar, D., Riquelme, S., Xu, X., Baez, J.C., Geng, J., Moreno, M. (2017). The first since 1960: a large event in the Valdivia segment of the Chilean Subduction Zone, the 2016 M7. 6 Melinka earthquake. Earth Planet. Sci. Lett. 474, 68–75.

Moreno, M., Melnick, D., Rosenau, M., Baez, J., Klotz, J., Oncken, O., al. (2012). Toward understanding tectonic control on the Mw 8.8 2010 Maule Chile earthquake, Earth and Planetary Science Letters, 321–322, 152–165. https://doi.org/10.1016/j.epsl.2012.01.006

Peña, C., Heidbach, O., Moreno, M., Bedford, J., Ziegler, M., Tassara, A., & Oncken, O. (2020). Impact of power-law rheology on the viscoelastic relaxation pattern and afterslip distribution following the 2010 Mw 8.8 Maule earthquake. Earth and Planetary Science Letters 542: 116292.

Press, W., A. Teukolsky, W. Vetterling, and B. Flannery (2002), Numerical Recipes in C: the Art of Scientific Computing, Cambridge Univ Press, Cambridge, U. K.

Ranalli, G. (1997). Rheology and deep tectonics. Ann. Geofis.XL (3), 671–780. https://doi .org /10 .4401 /ag -3893.

Tassara, A., Götze, H. J., Schmidt, S., and Hackney, R. (2006). Three-dimensional density model of the Nazca plate and the Andean continental margin. J. Geophys. Res. Solid Earth, 111(B9). DOI: 10.1029/2005JB003976

Wang, H.F., 2000. Theory of Linear Poroelasticity: With Applications to Geomechanics. Princeton University Press, Princeton.

Williamson, A.L. and Newman, A.V., (2018). Limitations of the resolvability of finite-fault models using static land-based geodesy and open-ocean tsunami waveforms. Journal of Geophy. Res.: Solid Earth, 123(10), pp.9033-9048